*Advanced Functional Materials*

ADVANCED FUNCTIONAL MATERIALS
www.afm-journal.de

RESEARCH ARTICLE OPEN ACCESS

# Meniscus Pixel Printing for Contact-Lens Vision Sensing and Robotic Control

Byung-Hoon Gong[1] | Dohyean Kim[1] | Jiyun Jeong[1] | Taekyeong Kim[1] | Soon-sung Kwon[1] | Junyoung Seo[1] | Il Jeon[2] | Im Doo Jung[3]

[1]Department of Mechanical Engineering, Ulsan National Institute of Science and Technology (UNIST), Ulsan, Republic of Korea | [2]Department of Nano Engineering, Department of Nano Science and Technology, SKKU Advanced Institute of Nanotechnology (SAINT), Sungkyunkwan University (SKKU), Suwon, Republic of Korea | [3]Department of Mechanical Engineering and Department of Graduate School of Artificial Intelligence, Ulsan National Institute of Science and Technology (UNIST), Ulsan, Republic of Korea

**Correspondence:** Im Doo Jung (idjung@unist.ac.kr)

**Received:** 30 November 2025 | **Revised:** 24 February 2026 | **Accepted:** 5 March 2026

**Keywords:** meniscus guided printing | pixelated contact lens | robot teleoperation | super resolution GAN | visual sensing

## ABSTRACT

Contact lenses are emerging as strong candidates for next-generation extended reality (XR) interfaces due to their lightweight and ergonomic form factor. However, integrating photodetector arrays onto the limited area of a lens remains challenging with conventional micropatterning approaches, which rely on masks, multistep processes, and specialized equipment that inherently limit throughput and scalability. To address these constraints, we introduce a Meniscus Pixel Printing (MPP) strategy that enables rapid, mask-free patterning of $MAPbI_3$ perovskite photodetectors without costly or complex fabrication tools. MPP uses a self-confined meniscus at a pipette tip to deterministically transfer perovskite ink, enabling 200 μm pixels to be printed within 1 s per pixel. In addition to planar substrates, MPP demonstrates stable pixel patterning on curved surfaces, highlighting its geometric adaptability and process versatility. Using this approach, we fabricate a $10 \times 10$ perovskite photodetector array and demonstrate stable photoresponse, retaining 92% of its initial performance after two months of storage. To overcome limited pixel density, a deep-learning-based super-resolution (SR) model reconstructs $10 \times 10$ inputs into $80 \times 80$ optical information with 97.2% accuracy and 0.03 s latency. Additionally, an AI-based eye-tracking system recognizes nine eye gestures with 99.3% accuracy, enabling smooth hands-free robotic arm control.

## 1 | Introduction

Virtual reality (VR), augmented reality (AR), and mixed reality (MR), collectively referred to as extended reality (XR), bridge physical and virtual environments and enable real-time monitoring, analysis, and simulation across a wide range of applications [1]. As XR-related technologies rapidly advance, demand for more immersive and interactive interfaces continues to grow in fields such as manufacturing, education, and healthcare. In particular, XR systems have shown strong potential in smart factory environments by improving product quality and enabling predictive maintenance [2, 3]. Commercial XR headsets, including Apple Vision, Meta Quest, and Microsoft HoloLens, have evolved substantially to meet these emerging demands. However, despite the technological progress in these devices, they still suffer from inherent limitations such as excessive weight, bulkiness, heat generation, and substantial power consumption [4–6]. These issues cause discomfort during extended use and restrict their

Byung-Hoon Gong and Dohyean Kim contributed equally to this work.

deployment in scenarios requiring continuous long-term operation [7]. This has driven significant interest in the development of lightweight and ergonomic wearable XR platforms, such as glasses-based systems and contact lens-based devices [8, 9].

Among these emerging form factors, contact lens has gained traction as an ultracompact platform capable of integrating displays, sensors, and communication modules, offering a promising alternative to conventional XR headsets. Prior studies have demonstrated functional contact lens systems such as Prussian blue-based electrochromic displays for AR navigation, VCSEL integrated lens and glasses architectures for holographic projection, and plasmonic etalon-structured lens for tear glucose monitoring [10–16]. A key requirement for enabling full XR capabilities in such devices is the integration of photodetectors that can sense and process external optical signals within the extremely limited surface area of the contact lens [17]. To address this need, various optical sensing materials have been explored, including silicon-based sensors for eye tracking and metal-based plasmonic structures for enhanced photoresponsivity [18–20]. Among these materials, perovskite has emerged as a highly promising candidate due to its strong visible light absorption, tunable bandgaps, long carrier diffusion lengths, and compatibility with low-temperature generation and low-power consumption during operation [21–25]. In particular, solution-processable perovskites such as $MAPbI_3$ offer substantial advantages over traditional semiconductors, including Si, CdS, $SnO_2$, and $TiO_2$, due to their ease of fabrication and suitability for scalable patterning [26–28].

Despite these material advantages, the incorporation of photodetectors into contact lens requires careful consideration of several design and operational constraints. In wearable vision systems, pixel area directly influences photon collection efficiency and signal-to-noise ratio (SNR), which becomes particularly critical under low-light conditions, as encountered in contact lens platforms [29, 30]. Given the severe limitations in sensing area, optical path length, and power budget, employing relatively large pixel sizes to secure sufficient light-receiving area represents a practical strategy for stable low-light imaging [31, 32]. Several patterned deposition techniques for perovskite materials have been reported, including meniscus-induced 3D nano-printing, inkjet printing, and meniscus-assisted solution printing. Meniscus-induced 3D nano-printing enables submicron-scale free-form perovskite structures with high spatial resolution. However, when fabricating submillimeter pixel arrays with sufficiently large active areas for reliable photodetection, the process relies on continuous line or zigzag trajectories, resulting in prolonged printing times and increased susceptibility to nozzle clogging due to solvent evaporation and solute precipitation during extended operation. These factors limit yield, repeatability, and practical scalability [33, 34]. Inkjet printing offers higher throughput via droplet-based micropatterning and has been widely employed for perovskite microstructure photodetector arrays [35]. Nevertheless, maintaining consistent pattern fidelity on curved or inclined substrates remains challenging due to variations in nozzle-to-substrate distance and the strong dependence on droplet landing dynamics. Additional process optimization is typically required to suppress lateral diffusion or sliding of deposited droplets [36, 37]. Electrohydrodynamic (EHD) printing further enhances patterning resolution through electric-field-assisted jetting. However, it generally requires a high-voltage power supply, and patterning versatility is constrained by its strong dependence on ink conductivity, substrate electrical properties, and nozzle-to-substrate distance [38]. Moreover, variations in local electric field strength on non-planar substrates can lead to unstable droplet formation, necessitating extensive optimization. To address geometric constraints associated with curved surfaces, McAlpine et al. demonstrated an extrusion-based printing approach [39]. However, this method is prone to capillary-driven relaxation and viscous flow following material extrusion, which leads to filament broadening and lateral spreading during deposition. This post-extrusion expansion restricts the achievable resolution, with reported feature diameters of approximately 1600 μm and pixel pitches of about 2500 μm. These dimensions are insufficient to meet the high-density integration requirements of contact lens imaging platforms. Meniscus-assisted solution printing enables uniform large-area perovskite film formation with controlled crystallization [40]. However, as a blade-coating-based technique, it is inherently unsuitable for individual pixel-level patterning necessary for imaging or vision-sensing arrays.

In parallel with these process-oriented efforts, complementary system-level strategies have also been investigated. Recent studies have explored the integration of perovskite photodetectors with algorithmic or AI-assisted reconstruction techniques to enhance imaging performance. Retina-inspired narrow-band perovskite sensor arrays combined with neuromorphic processing have demonstrated promising imaging capabilities, but higher spatial resolution in such systems is typically achieved by increasing sensor density, which enlarges device footprint and system complexity [41]. As an alternative to increasing hardware pixel counts, pixel imaging and single-pixel imaging approaches based on Fourier-domain or patterned illumination measurements have been reported using perovskite photodetector, enabling intelligent imaging, color sensing, and encrypted imaging functionalities with a limited number of physical pixels [42–44]. However, these approaches rely on iterative illumination with diverse optical patterns and sequential measurements, leading to prolonged acquisition time and substantial computational overhead for image reconstruction. Such characteristics limit their suitability for ergonomic wearable platforms that require immediate inference and real-time operation.

In this study, we address these limitations by introducing a Meniscus Pixel Printing (MPP) strategy that enables rapid, mask-free micro-patterning of perovskite photodetectors directly onto compact substrates without the need for lithographic masks or specialized equipment. In MPP, a stable meniscus formed between a pipette and the substrate mediates the transfer of perovskite ink, and the resulting pixel dimensions are precisely governed by controlled adjustments of the dwell time and the vertical displacement speed of the pipette. Using this approach, we fabricated a pixelated contact lens incorporating a micro-patterned $MAPbI_3$ photodetector array, which was subsequently encapsulated with a photocurable resin to enhance its mechanical robustness and resistance to moisture. To compensate for the inherently sparse pixel density of such compact arrays, we further proposed a deep-learning-based super-resolution (SR) framework capable of reconstructing high-resolution optical information from low-resolution perovskite pixel data. By integrating this platform with an incident light-based eye interaction scheme, the pixelated contact lens operates as a compact interface capable

of on-lens visual sensing, where external optical information is captured and enhanced through AI-driven reconstruction. Building upon this sensing capability, the system further enables robot teleoperation, in which eye movements are translated into control commands for external robotic devices. Through this combined hardware and software framework, the presented platform demonstrates how precise perovskite micro-patterning and AI processing can be unified within an ultralight wearable device. This approach outlines a scalable pathway toward next-generation wearable vision technologies and interactive XR interfaces.

## 2 | Results and Discussion

Figure 1a illustrates the schematic of the MPP process using perovskite ink. Perovskite ink inside a micro-nozzle pipette is brought into brief contact with an indium tin oxide (ITO) patterned substrate, where a confined meniscus forms between the nozzle tip and the surface. This meniscus acts as a controlled liquid bridge that regulates ink flow through capillary forces and interfacial tension, allowing material transfer to occur only within the narrow region defined by the meniscus geometry. Because the ink motion is governed by this self-limited capillary channel rather than by volume ejection, the process enables micro-scale patterning with high spatial precision and consistent dot dimensions without unnecessary ink consumption (Figure S1). The MPP process consists of four steps: approach and contact, meniscus formation, dwell time, and take-off, as captured by a real-time microscope camera in Figure 1b. A micro-nozzle pipette (inner diameter = 100 μm) approaches the ITO-patterned substrate and establishes physical contact. The pipette is then lifted slightly to stabilize the meniscus. At this stage, controlling the dwell time and nozzle speed allows fine adjustment of dot size. Figure 1c schematically illustrates how dwell time influences dot geometry, enabling patterned perovskite photodetectors to be formed within small electrode interfaces.

To pattern the photodetector within the confined region, we used $MAPbI_3$, which supports solution-based processing with controllable crystallization behavior and strong visible-light absorption. The solvent system consisted of N,N-dimethylformamide (DMF) and dimethyl sulfoxide (DMSO), both widely used for organic-inorganic hybrid perovskites. These solvents dissolve lead(II) halides (e.g., $PbI_2$, $PbBr_2$) and organic halides (e.g., MAI, FAI) to form intermediate complexes that regulate crystallization dynamics. As confirmed by the X-ray diffraction (XRD) patterns (Figure S2), films prepared with different solvent compositions exhibit distinct crystallographic orientations and relative peak intensities. Since solvent composition influences precursor complex formation, crystallinity, and defect passivation, the ink formulation was optimized to achieve improved device response. [45, 46]. The printed perovskite dots convert into fully crystallized $MAPbI_3$ through annealing, during which the solvent evaporates, crystallization progresses, and the film color changes from yellow to black (Figure 1d,e; Equation S1). The resulting absorbance spectrum shows strong visible-light absorption with an absorption edge near 780 nm (Figure S3a), and the extracted bandgap of ≈1.58 eV (Equations S2 and S3 and Figure S3b) agrees well with previously reported values for $MAPbI_3$ (1.5–1.6 eV) [47]. The scanning electron microscope (SEM) image further confirms the formation of sub-micron grains and successful MPP-based deposition on the patterned ITO substrate (Figure 1f).

Five ink formulations were evaluated by varying the DMF/DMSO solvent ratio (Figure 2a), and the ink yielding the highest photocurrent was selected for photodetector fabrication (Figure 2b). The photocurrent reached its maximum at a 3:1 ratio (2.58 μA), approximately twice that obtained using DMF alone (1.32 μA) under 100 mA illumination setting at a 3 V bias. This improvement arises from the distinct evaporation behaviors of the two solvents: DMF evaporates rapidly, and excessive DMF accelerates nucleation and disrupts uniform grain growth, producing smaller crystals with higher defect densities [48, 49]. In contrast, DMSO evaporates slowly, and its residual presence hinders charge transport within the perovskite layer [50]. To examine the rheological characteristics, the viscosity of DMF-only and DMF/DMSO mixed inks was measured using a rheometer (Figure 2c). Both inks exhibited near-Newtonian behavior, showing almost constant viscosity across shear rates from $10^1$ to $10^2$ $s^{-1}$, with values of ≈0.003 Pa·s (DMF only) and ≈0.005 Pa·s (DMF/DMSO mixture). Such Newtonian fluid characteristics provide stable meniscus formation during printing, enabling uniform, reproducible, and controllable dot patterning [14, 51]. The influence of solvent composition was further confirmed through morphological analysis: perovskite films prepared with DMF alone showed circular stain-like crystallization due to rapid evaporation, accompanied by non-uniform Pb and I distributions in energy dispersive X-ray spectroscopy (EDS) mapping (Figure 2d). In contrast, the DMF/DMSO mixed ink produced well-crystallized films with uniform elemental distribution, attributed to the slightly higher viscosity that suppresses convection and promotes controlled grain growth within the printed dots.

In the MPP process, precise control of dot size is essential for both device functionality and material efficiency, prompting a quantitative investigation of the effects of dwell time and nozzle speed. Figure 3a shows the top-view images of dots printed at various nozzle speeds (0.5, 1, 2, 4, 8 mm $s^{-1}$) and dwell times (0, 0.2, 0.4, 0.6, 0.8, 1 s) [52, 34]. The results demonstrate that adjusting these two parameters enables deterministic control of the dot diameter. As shown in Figure 3b, increasing the nozzle speed causes a systematic decrease in dot size, governed by the faster detachment of the meniscus during printing. In the capillary-dominated regime (We < 0.01), the reduced liquid-bridge lifetime at higher nozzle speeds limits the transferred volume before breakup, leading to a power-law dependence of dot radius on nozzle speed. In contrast, the dot diameter increases with dwell time due to capillary-driven meniscus flow while the nozzle remains in contact with the substrate. Under a quasi-steady approximation, the volumetric growth follows a $t^{1/3}$ scaling as the contribution of the droplet curvature to the Laplace pressure progressively diminishes. A more detailed physical description of the dot-growth mechanism is provided in the Supplementary Information (Section S1). During this period, the ink shape transitions from concave to convex, and increasing surface tension counteracts the pressure driving the ink outward, progressively slowing the extrusion rate. These observations confirm that coordinated tuning of nozzle speed and dwell time enables predictable dot size regulation in the MPP process. For example, a nozzle speed of 16 mm $s^{-1}$ with zero dwell time yields dot diameters of approximately 200 μm.

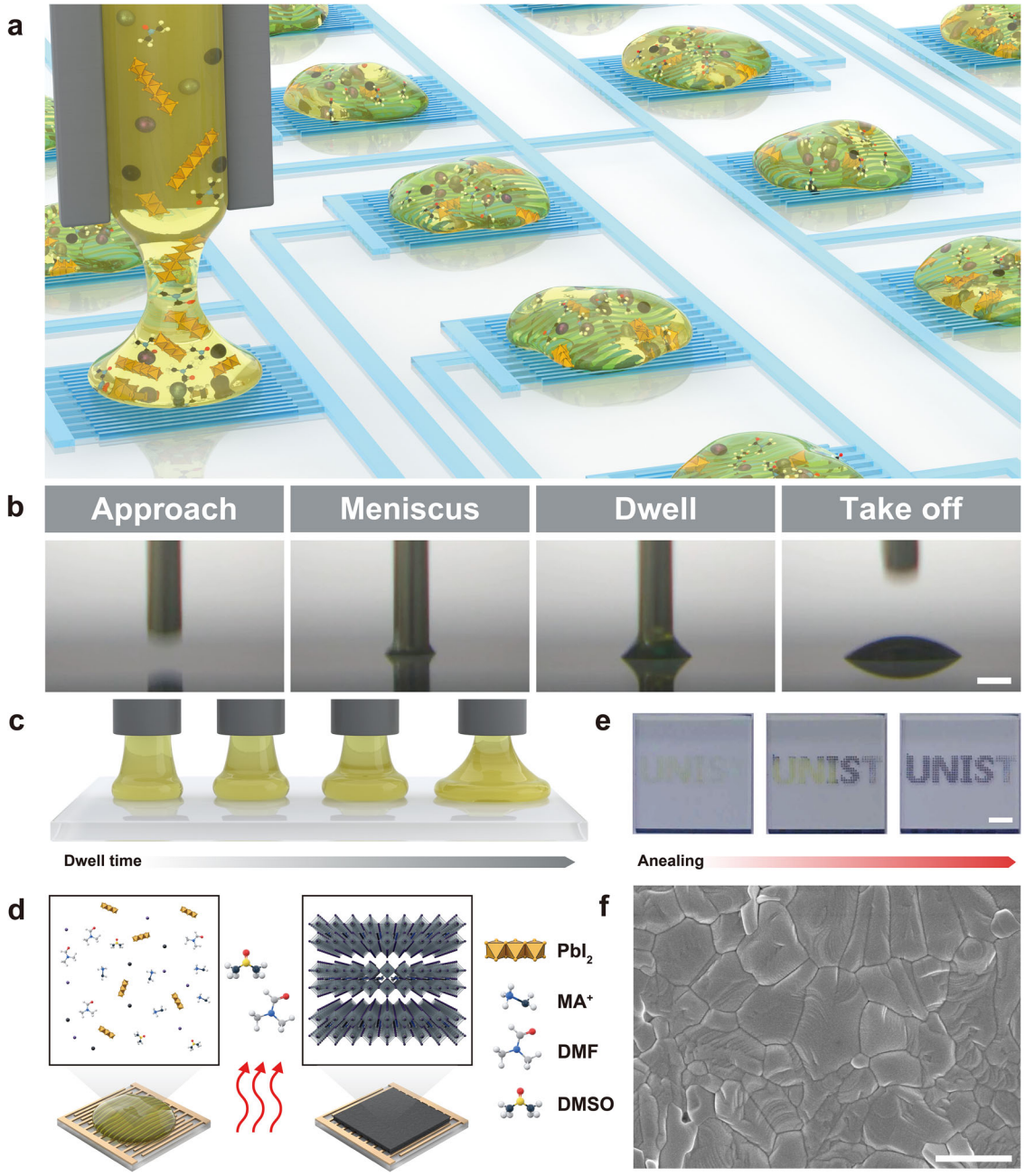


**FIGURE 1** | (a) Schematic of the MPP. (b) Optical images of the MPP process with a 100 μm nozzle on the substrate. The scale bar is 200 μm. (c) Conceptual illustration of dwell time-dependent dot sizes control. (d) Schematic of the Solution-mediated perovskite crystallization pathway following MPP. (e) The optical images show the crystallization during the annealing process. The scale bar is 5 mm. (f) SEM image of the resulting perovskite layer. The scale bar is 10 μm.

Figure 3c highlights the patterning capability and scalability of the MPP approach. A dot-patterned QR code was generated using a nozzle speed of 4 mm $s^{-1}$ and zero dwell time, demonstrating the ability of the method to precisely arrange large numbers of uniform dots. The word "UNIST" was also printed at a constant dot size while keeping a constant 16 mm $s^{-1}$ and zero dwell time (Movie S1), which enabled rapid and continuous fabrication of uniformly sized dots with considerable pattern consistency (Movie S2). The design flexibility of the MPP technique is further highlighted by the letter-dependent variations in dot arrangement, as demonstrated in each letter of the word "UNIST". Several iconic global landmarks were also reproduced with individual structure widths below 8 mm using a nozzle speed of 16 mm $s^{-1}$ and zero dwell time, confirming that MPP can reliably produce microscale pointillistic images with high spatial fidelity. All the pointillism results are annealed on the substrate, converting the ink dots into perovskite layers (Movie S3). These results show that the technique supports complex pattern generation and can be readily extended to applications such as artistic rendering or information encoding, including digital watermark within micro-scale patterns. Furthermore, to demonstrate the conformal compatibility of MPP, we performed patterning on substrates with a radius of curvature of 8.6 mm, which is comparable to the human pupil. Specifically, we demonstrated stable pixel printing

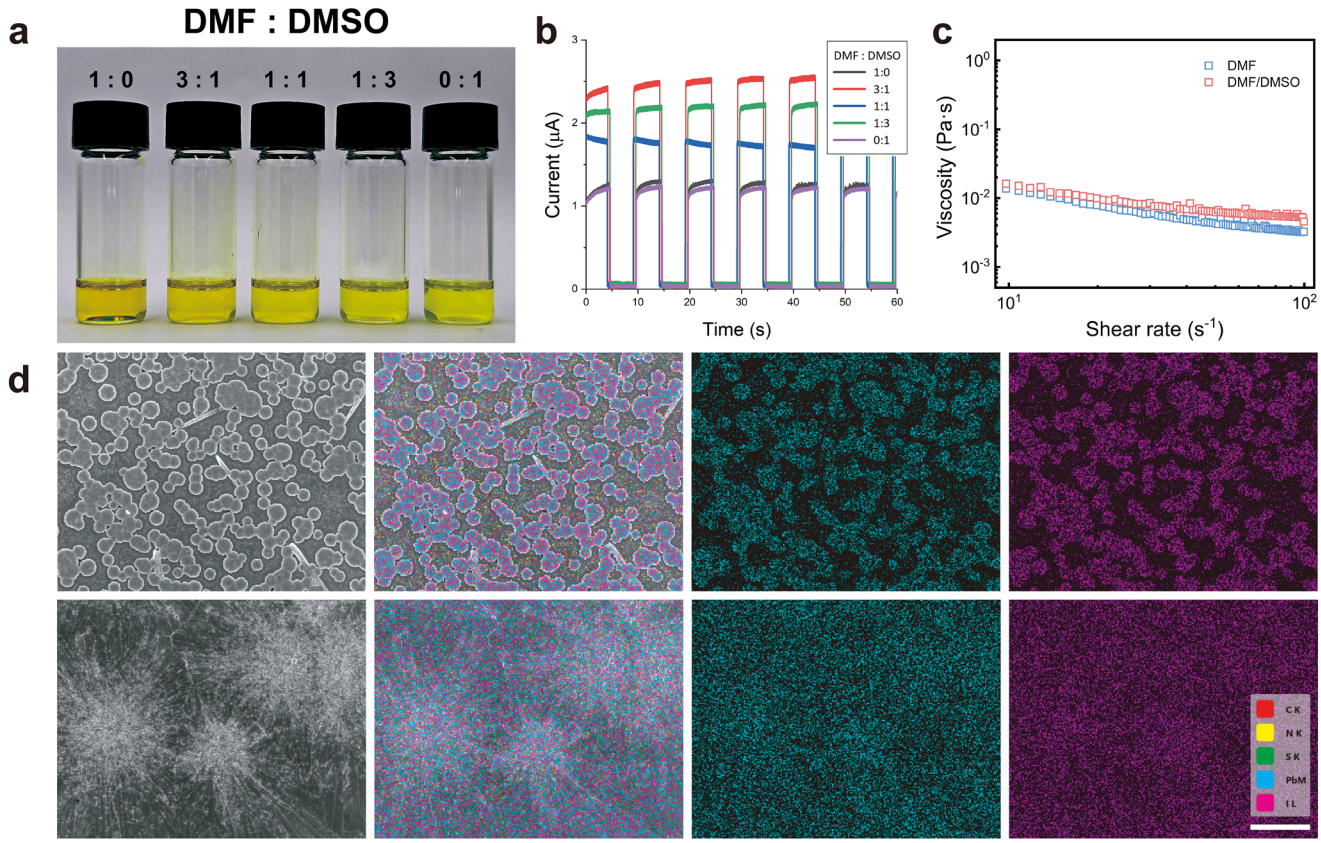


**FIGURE 2** | Perovskite inks, solvent-engineering, and results. (a) Inks with varied solution DMF/DMSO compositions. (b) Photocurrent response of the crystallized perovskite films under 680 nm LED illumination at 100 mA setting. (c) Viscosity of the perovskite inks. (d) SEM and EDS analyses of the perovskite layer fabricated using DMF-only ink (upper) and a mixture of DMF/DMSO ink (lower). The scale bar is 10 μm, and red means Carbon (C), yellow means Nitrogen (N), Green means Sulfur (S), Sky blue means lead (Pb), and purple means Iodine (I).

on surface slopes of up to 63.3° (Figure S4) and integrated 10 × 10 pixel arrays within 25 $mm^2$ as well as several global landmark patterns (Figure 3d). It presents that deterministic, pixel-level material deposition is possible with high positional fidelity even on steep slopes. These results highlight that MPP is a geometrically invariant pixel printing strategy capable of supporting both planar prototyping and curved device implementation without requiring architectural modifications, additional equipment, or process changes. It ensures robust process consistency, scalability, and compatibility with system-level integration, indicating that MPP is not merely an alternative to planar patterning techniques but a manufacturing-oriented approach that enables compact, curved photodetector arrays for wearable vision systems.

To integrate the perovskite photodetector onto the contact lens, which is a highly compact platform, an additional encapsulation step using a photocurable resin was introduced to protect the printed perovskite dots from moisture and mechanical damage after MPP deposition on the substrate. Figure 4a shows a top-view optical image of a uniformly patterned 10 × 10 perovskite photodetector array fabricated by MPP. The required dot diameter of 300 μm was reliably achieved using a nozzle speed of 4 mm $s^{-1}$ and a dwell time of 0 s as determined from the parameter study. Figure 4b shows an optical photograph of an eye-mimicking model with a pupil and sclera of human-relevant dimensions, onto which the fabricated visual-sensing contact lens is placed and electrically wired for sensing measurements. Figure 4c illustrates the cross-sectional structure of the pixelated contact lens under red illumination. The device exhibited clear photoresponse characteristics under 680 nm red light with a 0.1 Hz on/off modulation (Figure 4d), and the *I–V* curves obtained under varying LED drive currents (dark, 100, 300, and 500 mA) are presented in Figure 4e. The corresponding photocurrent measured at a 3 V bias (Figure 4f) increased approximately linearly with light intensity. The wavelength-dependent photocurrent and responsivity (Figure 4g,h) exhibit relatively strong responses in the red region, yet $MAPbI_3$ remains effective across the entire visible spectrum, consistent with its intrinsic optical characteristics (Figure S5). Long-term durability was evaluated through continuous 1-h operation and by retesting after two months of ambient storage. The device maintained stable output over the 1-h operation (Figure 4i), and after two months, retained approximately 92% of its initial photocurrent, with the average value decreasing from 1.17 to 1.05 μA (Figure 4j), whereas unprotected perovskite dots typically undergo rapid hydrolysis [53]. These results confirm that the photocurable resin encapsulation effectively preserves the structural and optoelectronic stability of the pixelated perovskite photodetector on the contact lens substrate. To further assess device reliability, thermal stability tests were performed to assess potential Joule heating during lens operation. The experiment was conducted using a thermal imaging camera (Hikmicro E01) to measure the surface temperature of the contact lenses after 10 h of continuous operation at a room temperature of 25°C. After 10 h, the lens surface temperature increases up to

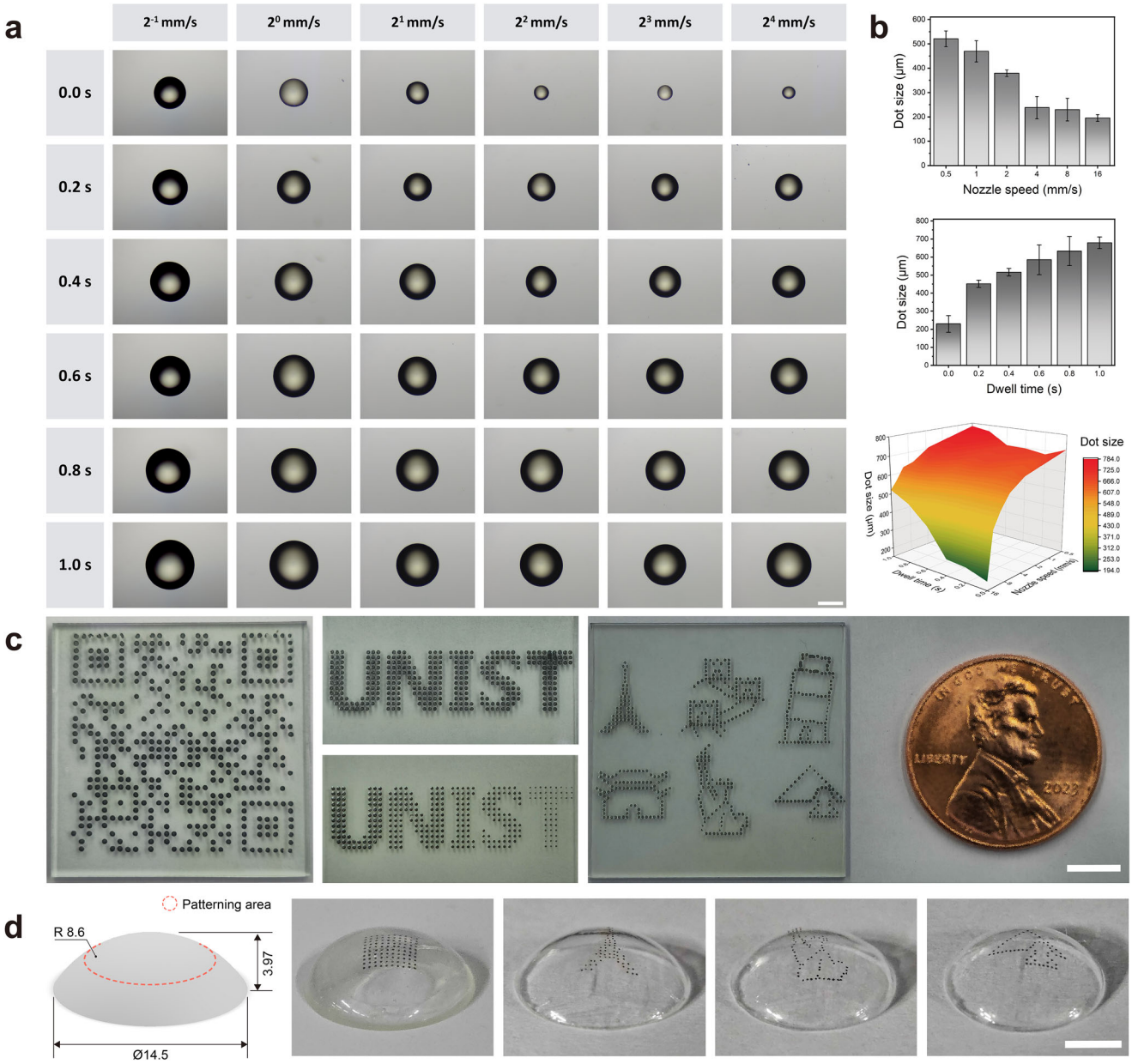


**FIGURE 3** | Relationship between printing parameters and dot formation behavior during the MPP process and optical pattern demonstrations. Scale bars are 5 mm. (a) Optical images of the MPP printed perovskite dots produced using a 100 μm nozzle under various nozzle speeds (0.5, 1, 2, 4, 8 mm $s^{-1}$) and dwell time (0, 0.2, 0.4, 0.6, 0.8, 1 s) conditions. The scale bar is 100 μm. (b) Dot diameter dependence on nozzle speed and dwell time, obtained from optical microscopy measurements (average and standard errors were calculated from six independent dots). Upper: fixed dwell time at 0.2 s. Middle: fixed nozzle speed at 8 mm $s^{-1}$. Lower: The 3D surface plot illustrates the correlation between dot size and the two printing parameters (nozzle speed and dwell time). (c) Printed pointillism images of QR code, dot-patterned 'UNIST' symbols with uniform and variable dot diameters, and representative world landmarks (Eiffel Tower, Great Wall, Tower of Pisa, Sungnyemun, Statue of Liberty, and Pyramid with Spinks). A U.S. penny (19.05 mm in diameter) is included to provide a visual size reference. (d) Printed pointillism images of a 10 × 10 grid within 25 $mm^2$ and representative world landmarks (Eiffel Tower, Statue of Liberty, and Pyramid with Spinks) on a curved substrate with a radius of curvature of 8.6 mm.

26.1°C, corresponding to an increase of 1.5°C (Figure S6). This temperature variation indicates effective thermal stability under prolonged operation and supports the feasibility of the device for wearable ocular applications. In addition, to evaluate potential lead leakage under mechanically stressed conditions relevant to rigid contact lens handling, fully encapsulated devices were subjected to cyclic compressive pressure tests while immersed in phosphate-buffered saline (PBS) at 37°C. A cyclic pressure of 30 kPa was applied for 100 cycles, corresponding to reported contact pressures during rigid lens insertion and removal. Inductively coupled plasma mass spectrometry (ICP-OES) analysis of the soaking solution revealed no detectable Pb ion concentration above the instrumental detection limit (2 ppb), indicating that the multilayer encapsulation effectively suppresses lead release even under repeated mechanical loading (Figure S7).

By using the pixelated contact lens as the sensing front end, we designed an optical sensing system capable of recovering optical

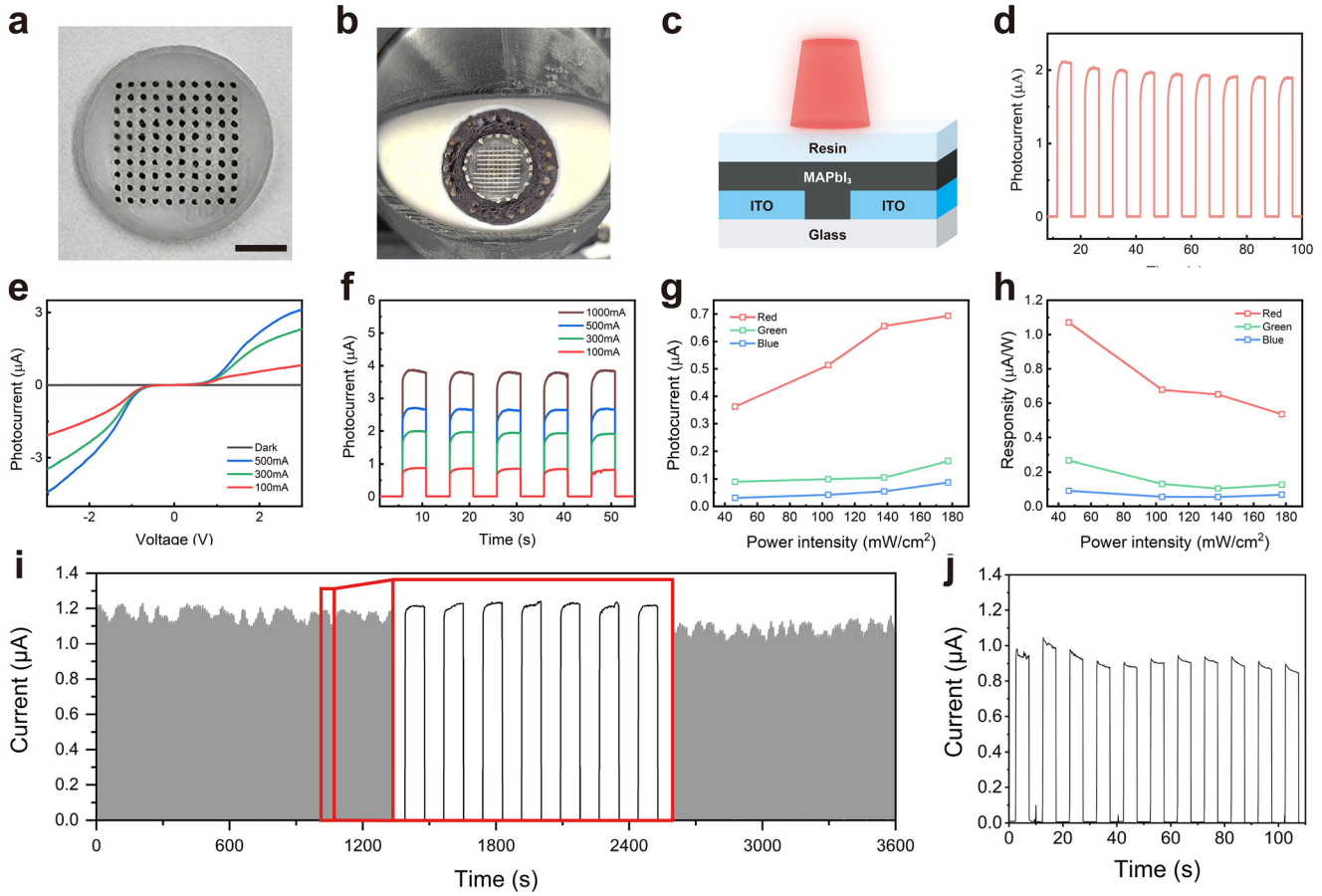


**FIGURE 4** | Structural configuration and optoelectronic performance of the pixelated contact lens with perovskite photodetectors. (a) Optical image of a fabricated pixelated contact lens with perovskite photodetector dots. The scale bar is 1 mm. (b) Optical image of the artificial eye module with a fabricated pixelated contact lens. (c) Cross-sectional schematic of the pixelated contact lens architecture. (d) Photocurrent response of an individual perovskite photodetector pixel under periodic on/off illumination. (e) Photocurrent, which is obtained by changing the 3 V of bias voltage at different LED settings (dark, 100 mA, 300 mA, and 500 mA). (f) Photocurrent output as a function of LED illumination settings (100 mA, 300 mA, 500 mA, and 1000 mA). (g) Wavelength-dependent photocurrent characteristics under red (680 nm), green (570 nm), and blue (380 nm) illumination. (h) Responsibility of the perovskite photodetector to different wavelengths. (i) One-hour continuous on/off switching examination results and view of the highlighted region. (j) Photocurrent performance after two months of exposure to the air.

information that is otherwise lost due to the limited number of photodetectors (Figure 5a). The inherently compact form factor of the contact lens fundamentally limits the number and density of sensors that can be integrated onto its surface. This causes the raw measurements to lack sufficient detail, making subtle variations in optical information difficult to distinguish and limiting shape recognition, tracking accuracy, and subsequent signal utilization. To address the resolution constraints of the 10 × 10 perovskite pixel array and recover fine-scale optical information lost at the hardware level, we implemented an AI-assisted reconstruction framework based on SR techniques. This configuration was deliberately designed to validate system-level integration between printed photodetectors and computational reconstruction under limited hardware resources, while maintaining the minimum spatial resolution necessary to demonstrate the practicality and scalability of the system. Our approach constructs a tailored Super-Resolution Generative Adversarial Network (SRGAN) to suit the characteristics of the pixelated perovskite contact lens [54]. The framework upscales the raw 10 × 10 sensor output to an 80 × 80 representation while preserving essential structural features, enabling downstream visual tasks that cannot be supported by the native sensor resolution. The generator is trained to learn spatial dependencies and optically relevant feature correlations from a large dataset, allowing it to infer structural details absent from the sparse 10 × 10 measurements. A discriminator, trained concurrently, evaluates the realism of the reconstructed outputs and provides adversarial feedback that encourages the generator to produce high-resolution images with physically consistent edges and contours (Figure 5b; Figure S8). Perceptual loss is additionally incorporated to maintain higher-order structural patterns that are not captured by pixel-wise losses alone [55]. Through this SR-based reconstruction process, the system effectively compensates for the severe spatial sparsity of the pixelated contact lens and yields high-fidelity optical information.

To evaluate system performance, a testbed was constructed comprising the pixelated contact lens, LED illumination sources, patterned masks, an artificial eye module, two microcontroller units, and custom control software (Figure 5c,d; Figure S9). In this setup, light emitted from the LEDs passed through a patterned mask to form specific optical shapes, which were subsequently

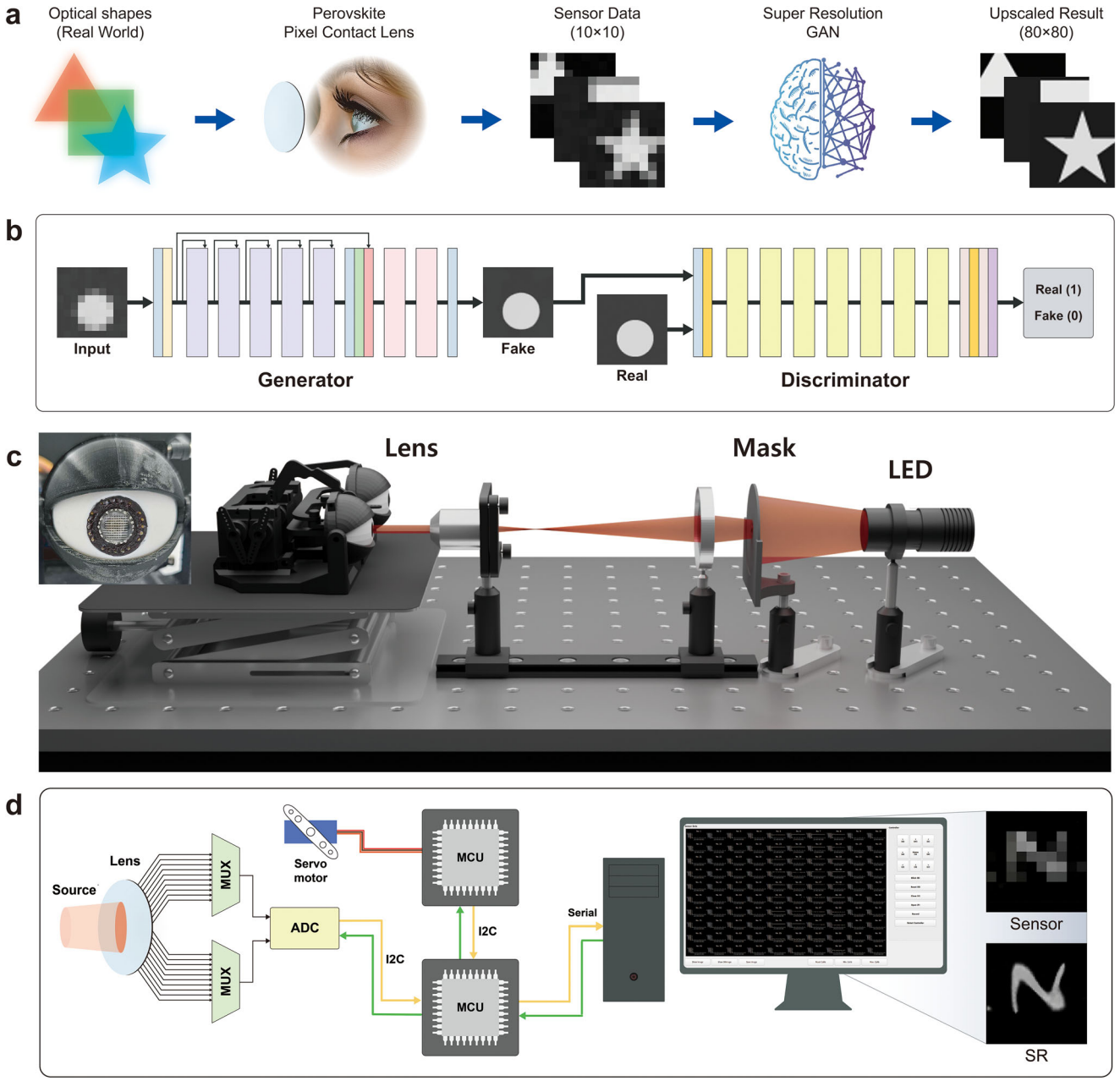


**FIGURE 5** | Implementation of an AI-assisted perovskite pixelated contact lens system. (a) Workflow of the deep learning-based pixelated contact lens system for high-resolution data sensing. (b) Schematic of the SRGAN model architecture. (c) Testbed schematic for verification of the pixelated contact lens system. (d) Circuit configuration diagram of the testbed.

detected by the contact lens. The artificial eye module, fabricated from 3D printed components and driven by servo motors, generated controlled movements in eight directions as well as eyelid blinking (Figure S10). One microcontroller handled data communication with the desktop via a multiplexer (MUX) and analog-to-digital converter (ADC), while the other controlled the motion of the artificial eye module. When training the SR model, we intentionally restricted the training dataset to seven primitive geometric classes (circle, triangle, square, star, heart, crescent, and cross) (Figure S11d). SR reconstruction was then evaluated using handwritten digits from the MNIST dataset [56], which were not included during training and extend beyond simple geometric patterns. For quantitative evaluation of the system's ability to enhance optical pattern recognition, a pretrained VGG19 network capable of classifying ten digits was employed as a classifier [57]. For this evaluation, optical datasets corresponding to 25 randomly sampled digit images per class from the MNIST test set were acquired. The measured data were upsampled using the SR model and subsequently classified by the VGG19 network, achieving a classification accuracy of 97.2% (Figure S12). This result indicates that discriminative structural information was preserved throughout the reconstruction process.

Representative comparisons between the raw 10 × 10 measurements and their corresponding super-resolved outputs are provided in Figure 6a and Movie S4. If the model were operating primarily as a classifier over a limited set of learned templates, such unseen composite or structurally distinct geometries would

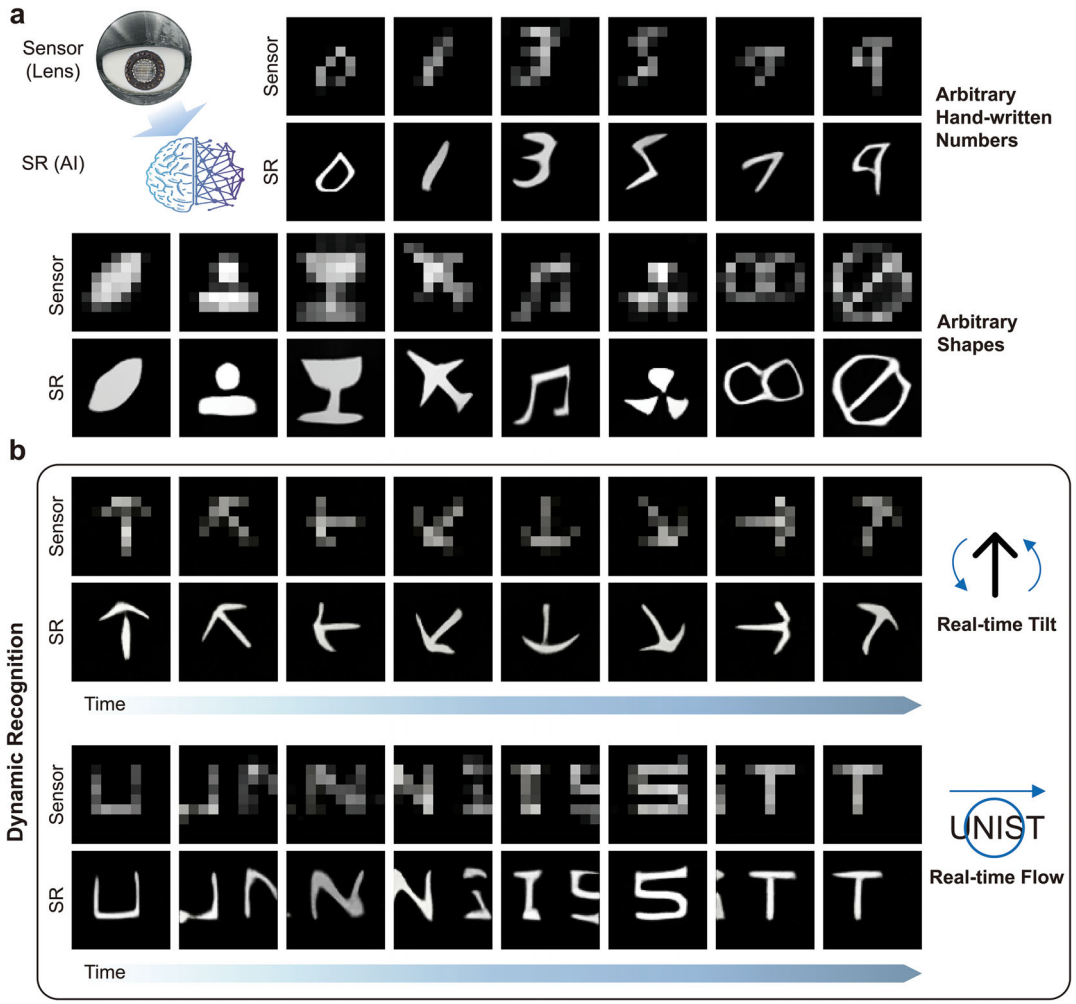


**FIGURE 6** | Representative comparison between the original 10 × 10 sensor data and the upscaled 80 × 80 results. (a) Arbitrary hand-written numbers and shapes. (b) Real-time dynamic reconstruction of a tilting arrow and shifting "UNIST" symbols.

be expected to collapse toward the closest trained prototypes. However, the model reconstructed stroke thickness, curvature, and structural variations of the digits. These results preserved the characteristic structures of each unseen pattern, indicating that the model reconstructs spatial information encoded in the measured optical signals. To further demonstrate that the system performs continuous reconstruction rather than discrete categorization, we evaluated dynamic visual inputs by continuously varying previously unseen patterns (Figure 6b; Movies S5 and S6). Specifically, arrow-shaped patterns were rotated through 360°, and the "UNIST" symbol was translated continuously across the field of view. The SR model accurately tracked these variations and reconstructed the corresponding geometries in real time. These results confirm that the proposed system performs signal-consistent SR reconstruction based on physical optical inputs, rather than relying on memorized shape categories, thereby supporting generalization to previously unseen and dynamically changing visual patterns. In addition, the proposed SRGAN model required approximately 0.03 s per inference on an Intel i7-1260P CPU, supporting real-time operation. These results indicate that integrating the pixelated contact lens with data processing via a deep learning algorithm enables a compact vision interface capable of producing high-resolution optical information despite the limited hardware footprint.

The AI-assisted pixelated contact lens system was further evaluated as a hands-free human-machine interface for eye movement-based robotic teleoperation. The overall configuration consisted of the contact lens module, the SR sensing system, an eye-tracking algorithm, and a WidowX 250 6DOF robotic arm (Figure 7a,b). As the eye moved, the incident-light distribution on the sensor shifted accordingly, and these frame-to-frame variations were analyzed to estimate the corresponding movement direction. To rigorously validate the effectiveness of the SR framework, the spatial resolution of the contact lens module was intentionally reduced from 10 × 10 to 5 × 5, thereby establishing a substantially more constrained sensing environment. Under this stringent condition, the reduced spatial resolution severely limited direct motion estimation, thereby requiring SR reconstruction to recover sufficient spatial information. To track eye movement, the super-resolved 80 × 80 data was binarized to isolate the optical region, after which the contour was extracted, and a minimum circumscribed circle was computed to extract the centroid (Figure 7c). Frame-to-frame changes in the centroid position were then mapped to nine discrete movement classes, including up, down, left, right, four diagonal directions, and blink. The algorithm was implemented based on an AI-tailored processing pipeline, with OpenCV serving as the underlying


**FIGURE 7** | Demonstration of eye-tracking and robotic teleoperation using the pixelated contact lens system. (a) Nine types of movements of the artificial eyes module. (b) Synchronized robot arm motion corresponding to eye movements. (c) Schematic diagram of the eye-tracking algorithm based on incident light. (d) Confusion matrix of eye-tracking results and visualization in the case of low-resolution (5 × 5) and high-resolution (80 × 80) data. (e) Robot arm teleoperation and pick-and-place demonstration based on an eye-tracking algorithm.

framework for contour extraction and geometric computation (Figure S13). The system was converted into joint commands or end-effector displacements for robotic control based on eye-tracking results. Both joint-level control and end-effector position control were implemented using forward and inverse kinematics to synchronize each directional category with the appropriate actuator behavior (Tables S1 and S2) [58]. The system was configured so that the direction estimated in each frame immediately triggered the corresponding robot action with minimal latency.

To compare the detection accuracy of optical variations at different resolutions, eye-tracking results obtained from both the raw and upscaled data were analyzed across nine eye-movement classes. For the raw data, the same algorithm was applied, except that the maximum-intensity pixel was used to estimate the center coordinate. A total of 50 experiments were conducted for each class to evaluate the correspondence between the estimated and actual eye movements. With the raw 5 × 5 measurements, the accuracy across the nine movement classes was 88.4% (Figure 7d), and most misclassifications occurred in

diagonal directions where subtle illumination differences could not be resolved at low pixel density. Such performance is insufficient for applications requiring high precision teleoperation, where misclassification could lead to operational failures or even equipment damage. In contrast, using the 80 × 80 upsampled data via SRGAN increased the accuracy to 99.3%, effectively eliminating directional confusion. This improvement arises from the detailed information recovered through the SR process. A pick-and-place task was conducted to verify the practical teleoperation capability of the system (Figure 7e; Figure S14 and Movie S7). Following the eye-tracking algorithm in real time, the robotic arm executed a sequence of picking and placing motions without the need for any physical controller. Because eye movements were translated into continuous control commands rather than discrete inputs, the interaction remained fluid and fully hands-free. These results demonstrate that the combination of the pixelated contact lens and AI-assisted SR enables reliable, real-time robotic manipulation driven solely by eye motion.

## 3 | Conclusion

This study demonstrates the MPP method as a rapid and precise micropatterning strategy capable of fabricating a 200-μm perovskite photodetector in 1 s without lithographic masking or specialized processing equipment. Owing to its intrinsically simple process configuration, MPP ensures broad applicability and practical scalability. Beyond its design versatility, the method enables deterministic positional control through direct nozzle–substrate contact, allowing high-fidelity pixel patterning. Moreover, its geometrically invariant and conformal characteristics support both planar prototyping and curved device integration without additional equipment or process modification (Table S4). Using this technique, a 10 × 10 perovskite photodetector array was integrated onto a compact substrate, establishing a miniaturized platform for visible-light sensing. To overcome the intrinsic resolution limitation of the 100-pixel array, a deep-learning-based SR sensing framework was developed to convert 10 × 10 inputs into 80 × 80 high-resolution outputs in real time, achieving 97.2% classification accuracy across diverse optical patterns. When integrated with an eye-tracking algorithm, the system further distinguished nine eye gestures with 99.3% accuracy, even under highly constrained sensing conditions, enabling real-time robotic teleoperation. Overall, these results demonstrate that ultrafast MPP fabrication, combined with its process simplicity and conformal adaptability, enables a compact, high-performance optical interface, providing a promising pathway toward lightweight XR systems, advanced robotic control, and next-generation wearable vision technologies.

## 4 | Experimental Section

### 4.1 | Preparation and Characterization of Perovskite Precursor

A 1M of perovskite precursor solution was prepared by dissolving Methylammonium iodide ($CH_3NH_3I$, Sigma–Aldrich) and lead (II) iodide ($PbI_2$, 99.9%, TCI Chemicals) at a 1:1 molar ratio. The perovskite precursor solution was prepared using five different DMF/DMSO solvent ratios to investigate the properties, specifically 1:0, 3:1, 1:1, 1:3, and 0:1. Inks were stirred on a hot plate with a magnetic stirrer at 60°C for 2 h. The rheological properties of the inks were characterized using a rheometer (Haake MARS III, ThermoElectron).

### 4.2 | Meniscus Pixel Printing (MPP)

The 100 μL of perovskite ink was loaded into a 3 mL syringe barrel (Musashi Engineering Inc.) and extruded through a micronozzle with an inner diameter of 100 μm at room temperature. The printing substrate was coated with indium tin oxide (ITO) with a resistance of 4–6 Ω $cm^{-2}$ (AMG Tech). Before the printing process, the ITO substrates were cleaned using ultrasonic cleaning in acetone, isopropanol (IPA), and deionized (DI) water for 10 min each. The printing was performed using a 3-axis (x, y, z) motion platform (SHOT mini 200SX, Musashi Engineering Inc.) to control the nozzle speed, dwell time, and position. The printing path was regulated using customized G-code, and the dot size was optimized by adjusting nozzle speed and dwell time. The process was monitored in situ with an ultra-high-speed camera (a2A4504-18ucBAS, BASLER). The printed perovskite dots were annealed on a hot plate at 100°C for 10 min to promote the formation of perovskite crystals.

### 4.3 | Photodetectors in Contact Lens

A patterned circular ITO substrate (diameter: 8 mm, thickness: 0.7 mm) was first prepared to achieve a pixelated contact lens. The patterned ITO electrodes were fabricated in a 10 × 10 array. Each individual electrode consists of 7 pairs of interdigital electrodes with a width of 10 μm and a gap of 10 μm. The area of each individual electrode is 270 × 310 $μm^2$. MPP was performed on each electrode with a nozzle velocity of 4 mm $s^{-1}$ and a dwell time of 0 s to fabricate 300 μm diameter of dots. After annealing, 1 μL of photocurable resin was drop-cast onto the printed dots to encapsulate the perovskite that is unstable in ambient conditions and cured using a UV lamp for 1 min. The photocurable resin was prepared by initially mixing 2.5 g of aliphatic urethane diacrylate (POLYGOMER PN-3260, Polyne Technology) and 1.5 g of isobornyl acrylate (Sigma–Aldrich) for 3 min. Subsequently, 0.012 g of phenylbis(2,4,6-trimethylbenzoyl)phosphine oxide (BAPO, Sigma-Aldrich) was added, and the mixture was further stirred for 2 min. The 25 individual electrodes and a common electrode were connected to enamel wires with silver paste to complete the final circuit configuration. The sensors are operating under 3 V of bias voltage.

### 4.4 | Characterization

The microscopic characteristics and elemental composition of the printed perovskite were analyzed using field-emission scanning electron microscopy (FE-SEM, SU8220, Hitachi). The printing resolution of the printed perovskite was evaluated using optical microscopy. The UV–vis absorption spectra and optical bandgap data were acquired using a UV–vis-NIR spectrophotometer (Cary 5000, Agilent Technologies) over a measurement range of 300–900 nm. Photodetector properties were investigated by measuring I-V characteristics, time-current response, and responsivity using

an AUTOLAB PGSTAT204 at room temperature. This measurement was obtained by varying the wavelength and intensity of the incident light. The incident lights used were 680 nm (Red), 530 nm (Green), and 470 nm (Blue) with intensity controlled through a high-power 1-channel LED driver (DC2200, Thorlabs).

### 4.5 | Implementation of a Testbed for the Pixelated Contact Lens System

A single Arduino Mega 2560 communicated with the ADC and MUX via inter-integrated circuit (I2C) to acquire the sensor data. The collected data were processed in real-time through kalman filter to remove the noise. And data was transferred to the desktop, normalized to a range of 0–1024 for image plotting after calibration using Python. Graphical user interface (GUI) visualized 10 × 10 sensor data and 80 × 80 data upsampled with SR models in real-time. The artificial eyes module was made by 3D printing and operated by SG90 servo motors. These motors were controlled by an Arduino Uno, which communicated with an Arduino Mega 2560 via I2C to receive operational commands.

### 4.6 | Artificial Intelligence Assisted Pixelated Contact Lens System

Since it is challenging to obtain high-resolution data pairs that precisely correspond to low-resolution sensor measurements, a data processing pipeline was constructed based on seven fundamental shape types to generate a sufficiently large training dataset (Figure S11). The pipeline incorporates various data augmentation techniques to capture the signal characteristics observed by the actual sensor, thereby embedding potential randomness and both internal and external system interferences into the training data. For each shape, 5,000 samples were generated, resulting in a total dataset of 35,000 instances used to train the SR model. In the validation process, an additional 7,000 samples were used to evaluate model performance by defining scores that allow integrated consideration of the Fréchet inception distance (FID) and peak signal-to-noise ratio (PSNR) (Section S2 and Figure S15). The model was implemented and trained using the PyTorch framework, and detailed specifications of the training procedure are provided in Table S3.

### 4.7 | Analysis of Recognition Accuracy of the Pixelated Contact Lens System

To evaluate the recognition accuracy of the upsampled data generated by the SR model, a VGG19-based classifier was employed to categorize the data into ten classes. The pre-trained VGG19 weights were loaded, and the feature extraction layers were frozen, while only the classifier layers were fine-tuned. The final layer of the classifier was modified to output predictions for the ten classes. The MNIST dataset was used for model training. The original training set was randomly split into training and validation sets with an 80:20 ratio, while the official test set was used for performance evaluation. For testing, the classification accuracy was determined by comparing the predicted class labels with the ground-truth labels. All model implementation and training were performed using the PyTorch framework.

#### Acknowledgements

This work was supported by the National Research Foundation (NRF) grant funded by the Korea government (MSIT) (Nos. RS-2023-00211636 and RS-2025-2453204), Institute of Information & communications Technology Planning & Evaluation (IITP) grant funded by the Korea government (MSIT) (No. 2020-0-01336, Artificial Intelligence Graduate School Program (UNIST)), and the Human Resources Development of the Korea Institute of Energy Technology Evaluation and Planning (KETEP) grant funded by the Korea government Ministry of Knowledge Economy (No. RS-2023-00240918).

#### Conflicts of Interest

The authors declare no conflict of interest.

#### Data Availability Statement

The data that support the findings of this study are available in the supplementary material of this article.

#### References

1. K. Kim, H. Yang, J. Lee, and W. G. Lee, "Metaverse Wearables for Immersive Digital Healthcare: A Review," *Advanced Science* 10 (2023): 2303234, https://doi.org/10.1002/advs.202303234.

2. M. Rostami, P. Pradhan, N. Karki, et al., "A Comprehensive Review of Extended Reality and its Application in Aerospace Engineering," *Progress in Aerospace Sciences* 157 (2025): 101118, https://doi.org/10.1016/j.paerosci.2025.101118.

3. N. Alam, N. Saha, V. Gadow, R. Harik, and J. Ryu, "Role of Extended Reality (XR) Technologies in Maintenance Operations: Trends, Challenges, and Integration in Industry 4.0," *Manufacturing Letters* 44 (2025): 1545.

4. W. Q. Wu, X. D. Wang, X. Han, et al., "Flexible Photodetector Arrays Based on Patterned $CH_3NH_3PbI_{3-X}Cl_X$ Perovskite Film for Real-Time Photosensing and Imaging," *Advanced Materials* 31 (2019): 1805913, https://doi.org/10.1002/adma.201805913.

5. B. J. Park, S. J. Hunt, G. J. Nadolski, and T. P. Gade, "Augmented Reality Improves Procedural Efficiency and Reduces Radiation Dose for CT-Guided Lesion Targeting: A Phantom Study Using HoloLens 2," *Scientific Reports* 10 (2020): 18620, https://doi.org/10.1038/s41598-020-75676-4.

6. T. S. Perry, "Look Out for Apple's AR Glasses With Head-up Displays, Cameras, Inertial Sensors, and Lidar on Board, Apple's Augmentedreality Glasses Could Redefine Wearables," *Ieee Spectrum* 58 (2021): 26–54.

7. K. R. Pyun, J. A. Rogers, and S. H. Ko, "Materials and Devices for Immersive Virtual Reality," *Nature Reviews Materials* 7 (2022): 841–843, https://doi.org/10.1038/s41578-022-00501-5.

8. G. Mercier, E. O. Polat, S. T. Shi, et al., "Semitransparent Image Sensors for Eye-Tracking Applications," *Acs Photonics* 10 (2023): 2994–3000, https://doi.org/10.1021/acsphotonics.3c00473.

9. Y. M. Hu, T. Q. Wu, H. L. Guo, et al., "Perovskite-Based Smart Eyeglasses as Noncontact Human-Computer Interaction," *Advanced Materials* 37 (2025): 2412329, https://doi.org/10.1002/adma.202412329.

10. J. Kim, M. Kim, M. S. Lee, et al., "Wearable Smart Sensor Systems Integrated on Soft Contact Lenses for Wireless Ocular Diagnostics," *Nature Communications* 8 (2017): 14997, https://doi.org/10.1038/ncomms14997.

11. Y. Z. Zhu, S. P. Li, J. H. Li, et al., "Lab-on-a-Contact Lens: Recent Advances and Future Opportunities in Diagnostics and Therapeutics," *Advanced Materials* 34 (2022): 2108389, https://doi.org/10.1002/adma.202108389.

12. H. Seo, W. G. Chung, Y. W. Kwon, et al., "Smart Contact Lenses as Wearable Ophthalmic Devices for Disease Monitoring and Health Management," *Chemical Reviews* 123 (2023): 11488.

13. H. T. Zhu, H. Yang, S. Q. Xu, et al., "Frequency-Encoded Eye Tracking Smart Contact Lens for Human-Machine Interaction," *Nature Communications* 15 (2024): 3588, https://doi.org/10.1038/s41467-024-47851-y.

14. J. H. Kim, S. Park, J. Ahn, et al., "Meniscus-Guided Micro-Printing of Prussian Blue for Smart Electrochromic Display," *Advanced Science* 10 (2023): 2205588, https://doi.org/10.1002/advs.202205588.

15. F. M. Robert, B. Abiven, M. Sinou, et al., "Contact Lens Embedded Holographic Pointer," *Scientific Reports* 13 (2023): 6919, https://doi.org/10.1038/s41598-023-33420-8.

16. N. Roostaei and S. M. Hamidi, "Plasmonic Smart Contact Lens Based on Etalon Nanostructure for Tear Glucose Sensing," *Scientific Reports* 15 (2025): 14948, https://doi.org/10.1038/s41598-025-99624-2.

17. J. Park, H. Seung, D. C. Kim, M. S. Kim, and D. H. Kim, "Unconventional Image-Sensing and Light-Emitting Devices for Extended Reality," *Advanced Functional Materials* 31 (2021): 2009281, https://doi.org/10.1002/adfm.202009281.

18. L. X. Kong, G. L. Li, Q. Su, et al., "Inkjet-Printed, Large-Area, Flexible Photodetector Array Based on Electrochemical Exfoliated $MoS_2$ Film for Photoimaging," *Advanced Engineering Materials* 25 (2023): 2200946, https://doi.org/10.1002/adem.202200946.

19. L. Massin, V. Nourrit, C. Lahuec, et al., "Development of a New Scleral Contact Lens with Encapsulated Photodetectors for Eye Tracking," *Optics Express* 28 (2020): 28635–28647, https://doi.org/10.1364/Oe.399823.

20. H. J. Liu, Z. C. Chen, Y. C. Chang, and C. Y. Wu, "Plasmon-Enhanced Photoresponsivity and Detectivity of Silver Nanoparticles-incorporated Nanocomposites Flexible Photodetector," *Sensors and Actuators a-Physical* 379 (2024): 115923, https://doi.org/10.1016/j.sna.2024.115923.

21. J. B. You, Z. R. Hong, Y. Yang, et al., "Low-Temperature Solution-Processed Perovskite Solar Cells with High Efficiency and Flexibility," *Acs Nano* 8 (2014): 1674–1680, https://doi.org/10.1021/nn406020d.

22. M. R. Filip, G. E. Eperon, H. J. Snaith, and F. Giustino, "Steric Engineering of Metal-Halide Perovskites with Tunable Optical Band Gaps," *Nature Communications* 5 (2014): 5757, https://doi.org/10.1038/ncomms6757.

23. A. A. Zhumekenov, M. I. Saidaminov, M. A. Haque, et al., "Formamidinium Lead Halide Perovskite Crystals with Unprecedented Long Carrier Dynamics and Diffusion Length," *Acs Energy Letters* 1 (2016): 32–37, https://doi.org/10.1021/acsenergylett.6b00002.

24. S. Lim, M. Ha, Y. Lee, and H. Ko, "Large-Area, Solution-Processed, Hierarchical $MAPbI_3$ Nanoribbon Arrays for Self-Powered Flexible Photodetectors," *Advanced Optical Materials* 6 (2018): 1800615, https://doi.org/10.1002/adom.201800615.

25. X. Z. Xu, Y. T. Xiong, W. F. Liu, et al., "Tunable Fabrication of $MAPbX_3$ Triangular-Micro-Wires Array for Constructing High Sensitivity Photodetector," *Advanced Materials Technologies* 8 (2023): 2300946, https://doi.org/10.1002/admt.202300946.

26. W. C. Xiang, J. H. Zhang, S. Z. Liu, S. Albrecht, A. Hagfeldt, and Z. W. Wang, "Intermediate Phase Engineering of Halide Perovskites for Photovoltaics," *Joule* 6 (2022): 315–339, https://doi.org/10.1016/j.joule.2021.11.013.

27. Y. Wang, Y. Liu, S. Cao, and J. Wang, "A Review on Solution-Processed Perovskite/Organic Hybrid Photodetectors," *Journal of Materials Chemistry C* 9 (2021): 5302–5322.

28. L. D. Li, S. Ye, J. L. Qu, F. F. Zhou, J. Song, and G. Z. Shen, "Recent Advances in Perovskite Photodetectors for Image Sensing," *Small* 17 (2021): 2005606, https://doi.org/10.1002/smll.202005606.

29. S. Lee and S. Kim, "DDR-Net: Dual-Stream for Degraded Infrared Image Restoration Network," *IEEE Access* 13 (2025): 206531–206546.

30. C. Liu, A. Berkovich, Q. Chao, et al., "*Intelligent vision sensors for ar/vr*," (Optica Publishing Group, 2020).

31. K. Morioka, M. Osashima, N. Azuma, et al., "Development of a Fluorescence Microplate Reader Using an Organic Photodiode Array with a Large Light Receiving Area," *Talanta* 238 (2022): 122994.

32. D. Gregorek, A. Tibebu, E. Caudet, C. Barrera, and R. Bachmayer, "Long-Endurance Optical Seafloor Imaging Using Underwater Gliders: Concept, Development and Initial Trials," 2023 IEEE/RSJ International Conference on Intelligent Robots and Systems (IROS) IEEE, (2023).

33. M. Chen, S. Hu, Z. Zhou, et al., "Three-Dimensional Perovskite Nanopixels for Ultrahigh-Resolution Color Displays and Multilevel Anticounterfeiting," *Nano Letters* 21 (2021): 5186–5194.

34. R. Cai, H. Wang, X. Han, and D. Wang, "Meniscus-Guided 3D Printing with Material Supplied by the intrinsic Capillary Replenishment Flow: Printing Success Rate, Printed Structure Size Adjustment, and Microscale Functional Device Fabrication," *Journal of Materials Processing Technology* 339 (2025): 118822.

35. Y. Liu, F. Li, C. Perumal Veeramalai, et al., "Inkjet-Printed Photodetector Arrays Based on Hybrid Perovskite $CH_3NH_3PbI_3$ Microwires," *Acs Applied Materials & Interfaces* 9 (2017): 11662–11668.

36. S. M. Khalil, S. Ali, V. D. Nguyen, D. H. Cho, and D. Byun, "High-Precision Drop-on-Demand Printing of Charged Droplets on Nonplanar Surfaces with Machine Learning," *Advanced Intelligent Systems* 7 (2025): 2400621.

37. J. Yue, T. Gao, W. Zhang, et al., "Velocity-Adaptive Electrohydrodynamic Printing for Microscale Conformal Circuits on Freeform Curved Surfaces," *Acs Applied Materials & Interfaces* 17 (2025): 12883–12898.

38. L. Lu, Y. Zhou, J. Li, M. Si, and G. Ye, "Electrohydrodynamic Printing of Functional Inks for Flexible Electronics: Mechanisms, Materials, and Applications," *Advanced Materials Technologies* (2026): 02339.

39. S. H. Park, R. Su, J. Jeong, et al., "3D Printed Polymer Photodetectors," *Advanced Materials* 30 (2018): 1803980.

40. M. He, B. Li, X. Cui, et al., "Meniscus-Assisted Solution Printing of Large-Grained Perovskite Films for High-Efficiency Solar Cells," *Nature Communications* 8 (2017): 16045.

41. Y. Hou, J. Li, J. Yoon, et al., "Retina-Inspired Narrowband Perovskite Sensor Array for Panchromatic Imaging," *Science Advances* 9 (2023): ade2338.

42. X. Feng, C. Li, J. Song, et al., "Differential Perovskite Hemispherical Photodetector for Intelligent Imaging and Location Tracking," *Nature Communications* 15 (2024): 577.

43. Z. Zhang, P. Zheng, S. S. Yan, et al., "Ultrasensitive Perovskite Photodetector for Filter-Free Color Single-Pixel Imaging," *Advanced Optical Materials* 11 (2023): 2201847.

44. C. Li, W. Li, H. Hu, J. Zong, and H. Wei, "Lead-Free Perovskite Hemispherical Photodetector for Single-Pixel Imaging Encryption and Trajectory Tracking," *Nano Letters* 25 (2025): 13235–13242.

45. A. J. Doolin, R. G. Charles, C. S. De Castro, et al., "Sustainable Solvent Selection for the Manufacture of Methylammonium Lead Triiodide ($MAPbI_3$) Perovskite Solar Cells," *Green chemistry* 23 (2021): 2471–2486.

46. N. J. Jeon, J. H. Noh, Y. C. Kim, W. S. Yang, S. Ryu, and S. I. Seok, "Solvent Engineering for High-Performance Inorganic-Organic Hybrid Perovskite Solar Cells," *Nature Materials* 13 (2014): 897–903, https://doi.org/10.1038/Nmat4014.

47. A. M. A. Leguy, P. Azarhoosh, M. I. Alonso, et al., "Experimental and Theoretical Optical Properties of Methylammonium Lead Halide Perovskites," *Nanoscale* 8 (2016): 6317–6327, https://doi.org/10.1039/c5nr05435d.

48. Y. J. Jeon, S. Lee, R. Kang, et al., "Planar Heterojunction Perovskite Solar Cells with Superior Reproducibility," *Scientific Reports* 4 (2014): 6953, https://doi.org/10.1038/srep06953.

49. F. Guo, W. X. He, S. D. Qiu, et al., "Sequential Deposition of High-Quality Photovoltaic Perovskite Layers via Scalable Printing Methods,"

*Advanced Functional Materials* 29 (2019): 1900964, https://doi.org/10.1002/adfm.201900964.

50. Y. Bai, S. Xiao, C. Hu, et al., "A Pure and Stable Intermediate phase is Key to Growing Aligned and Vertically Monolithic Perovskite Crystals for Efficient PIN Planar Perovskite Solar Cells with High Processibility and Stability," *Nano Energy* 34 (2017): 58–68, https://doi.org/10.1016/j.nanoen.2017.02.019.

51. Y. Ma, C. Liu, M. Zhang, and Y. Mai, "Review on the Effects of Solvent Physical Properties on the Performance of Slot-Die Coated Perovskite Solar Cells," *Surface Science and Technology* 2 (2024): 25.

52. O. Loh, R. Lam, M. Chen, et al., "Nanofountain-Probe-Based High-Resolution Patterning and Single-Cell Injection of Functionalized Nanodiamonds," *Small* 5 (2009): 1667–1674, https://doi.org/10.1002/smll.200900361.

53. M. Mativenga, J. Ji, N. T. T. Hoang, and F. Haque, "Ambient Air Stability of Hybrid Perovskite Thin-Film Transistors by Ambient Air Processing," *Advanced Materials Interfaces* 7 (2020): 1901777, https://doi.org/10.1002/admi.201901777.

54. C. Ledig, L. Theis, and F. Huszár, "Photo-Realistic Single Image Super-Resolution Using a Generative Adversarial Network," in Proceedings of the IEEE Conference on Computer Vision and Pattern Recognition (2017).

55. J. Johnson, A. Alahi, and L. Fei-Fei, *Perceptual Losses for Real-Time Style Transfer and Super-Resolution* (Springer International Publishing, 2016).

56. Y. LeCun, "The MNIST database of handwritten digits," http://yann.lecun.com/exdb/mnist/, 1998.

57. K. Simonyan and A. Zisserman, "Very deep convolutional networks for large-scale image recognition," preprint, arXiv, September 4, 2014, https://doi.org/10.48550/ARXIV.1409.1556.

58. S. Wiznitzer, L. Schmitt, and M. Trossen, Interbotix ros manipulators, accessed July, 2025, https://github.com/Interbotix/interbotix_ros_manipulators.

## Supporting Information

Additional supporting information can be found online in the Supporting Information section.

**Supporting File 1**: adfm74852-sup-0001-SuppMat.docx.

**Supporting File 2**: adfm74852-sup-0002-movies1 for revision.mp4.

**Supporting File 3**: adfm74852-sup-0003-movies2 for revision.mp4.

**Supporting File 4**: adfm74852-sup-0004-movies3 for revision.mp4.

**Supporting File 5**: adfm74852-sup-0005-movies4 for revision.mp4.

**Supporting File 6**: adfm74852-sup-0006-movies5 for revision.mp4.

**Supporting File 7**: adfm74852-sup-0007-movies6 for revision.mp4.

**Supporting File 8**: adfm74852-sup-0008-movies7 for revision.mp4.